Laser Physics, Vol. 13, No. 5, 2003, pp. 711–723.

Optoacoustic Tomography: New Modality of Laser Diagnostic Systems

A. A. Karabutov[1], E. V. Savateeva[2], and A. A. Oraevsky[2]

[1] *International Laser Center of Moscow State University, Moscow, 119992, Russia*
[2] *University of Texas Medical Branch at Galveston, TX, 77555, USA*
e-mail: aak@sasha.phys.msu.su
Received September 16, 2002

Abstract—The current status of optoacoustic tomography for medical applications is reviewed. For 1D optoacoustic tomography, forward and backward modes of optoacoustic signal detection are discussed. To enhance lateral resolution of 1D tomography, a confocal optoacoustic transducer was developed and explored. The spatial resolution of 1D optoacoustic tomography is discussed. The applications of 1D optoacoustic tomography for the investigation of biological tissue are presented. A real-time 2D laser optoacoustic imaging system is described. The spatial resolution of 2D optoacoustic tomography is discussed. Some medical applications of 2D optoacoustic tomography are reviewed.

1. INTRODUCTION

Time-resolved optoacoustic tomography (OAT) is a rapidly developing technique for investigation of inhomogeneous objects. The interest in OAT is mostly connected with the successful results in cancer diagnostics obtained over the past few years. OAT combines advantages of pronounced optical contrast between different tissues and high resolution of wide-band ultrasound imaging. Laser pulses may be effectively used to produce acoustic waves in tissue with different optical absorption. Ultrasonic waves can propagate in biological tissue with minimal distortion and deliver diagnostic information to the surface of the tissue, where they may be detected with high temporal resolution by piezoelectric transducers.

Optoacoustic (OA) effect was discovered by Bell in [1] (1880). The first application of this phenomenon was for the measurement of IR absorption in gases [2] (1938). Investigation of the dynamics of excited molecules was performed in [3] (1946). Pulsed lasers open a new area in optoacoustics. Pioneers in this field were Askar'yan, Prokhorov, Chanturiya, and Shipulo [4] (1963). White [5] (1963) proposed the theory of thermal excitation of acoustic transients due to surface absorption of short electromagnetic bursts.

The dependence of the temporal shape of an OA signal on the value of the light absorption coefficient was established in the first experimental investigation of laser-matter interaction using a time-resolved optoacoustic method performed by Carome, Clark, and Moeller in [6] (1964). The lack of a theoretical basis, however, did not allow them to obtain quantitative results. The first attempt to give a theoretical explanation of the profile of the OA transient was given by Cleary and Hamrick [7] (1968). The relationship between the spatial distribution of heat sources and the temporal shape of the acoustic signal excited by a laser pulse was first theoretically analyzed in [8, 9]. The method for measuring the light absorption coefficient from the shape of an OA signal excited therein was first suggested and experimentally realized in [10, 11] and was later used in [12–16] for biological tissues. Time-resolved detection of an OA signal excited by a laser pulse in a medium under examination provides information on the spatial distribution of the optical properties of tissue. This is the basis of OAT.

When a laser pulse is absorbed by a medium, instant thermal expansion takes place. This thermal expansion gives rise to an acoustic transient. The amplitude and shape of the transient is defined by the parameters of the laser pulse and properties of the medium. When the laser pulse is short enough (shorter than the transit time of the acoustic wave over the light penetration depth, the so-called condition of stress confinement), acoustic transients resemble an absorbed energy distribution. So optoacoustic tomography uses the inherent optical contrast of tissue structure.

In [17] (1981), Wolbarsht proposed the use of OAT for diagnosing eye disease. The first experimental reconstruction of the light absorption coefficient distribution in a layered medium with the shape of an OA signal was performed in 1987 (details of these experiments can be found in [18]). The medium comprised a set of glass plates separated by layers of aqueous solutions of $CuCl_2$ of different concentrations, which caused a spatially inhomogeneous absorption of Nd:YAG laser radiation. An acoustic wave was detected on the side opposite to the exposed one of the stack (forward mode detection). Variation of the solution concentration in different layers changed the shape of the OA signal. Using the analytical relationships obtained earlier in [8], the light absorption coefficient distribution was calculated from the shape of this signal. The measured distribution of light absorption coin-

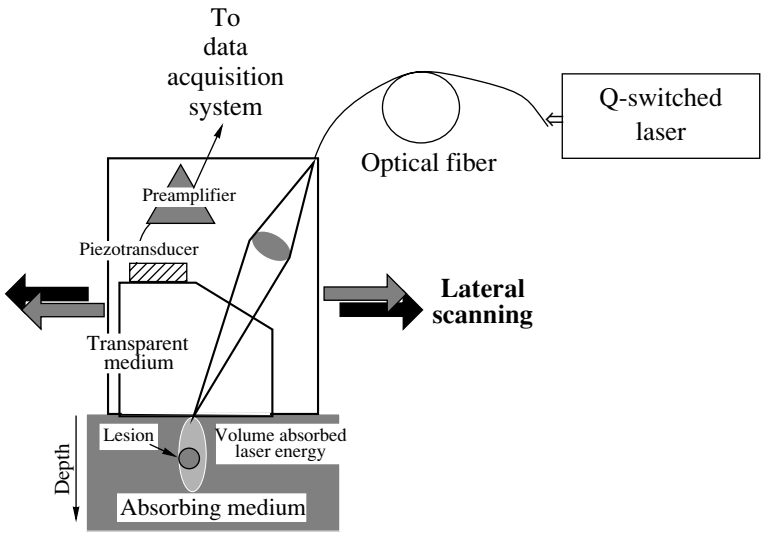

Fig. 1. Principles of OA imaging in backward mode.

cided well with the actual one. Similar experiments, with the collagen gel layers differing in the concentration of a dye, were described in [15, 16]. For different biological applications, the medium of interest is, as a rule, accessible from one side only. This gave rise to a new type of diagnostic technique: 1D OAT in backward mode. In this case, the acoustic transducer is placed at the same surface of the medium under investigation irradiated by laser. This technique was suggested in [15, 16] and independently realized in [19, 20]. The first theoretical model of light absorption reconstruction using the backward mode of OA-signal detection was proposed in [21]. In that work, 1D OA tomography was experimentally realized with a Q-switched Nd:YAG laser and a wide-band piezoelectric transducer. The time-resolved optoacoustic technique allowed investigation of light absorption in homogeneous media ($CuCl_2$ and milk solutions), macroinhomogeneous media (magnetic liquid), and microinhomogeneous media (carbon-black particles immersed in water and a $CuCl_2$ aqueous solution). The distribution of the light absorption coefficient for these media was calculated. These results are apparently the first successful application of 1D OA tomography in backward mode for the investigation of inhomogeneous media. A detailed theory on a laser of OA transients and its transformation in the course of propagation in a backward mode was given in [22]. The presented experimental OA signals were in good agreement with those predicted theoretically.

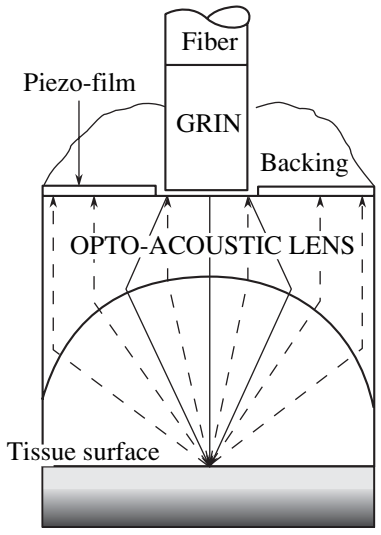

Fig. 2. Scheme of Confocal Optoacoutic Transducer (CONOAT).

Thus the theoretical background of laser OAT and reliability of the experimental techniques were developed and applications of laser OAT started. In this paper, we will consider only two rapidly growing branches of OA tomography: confocal optoacoustic microscopy (COAM) and a laser optoacoustic imaging system (LOIS). Advances in the former branch are presented in [23, 24]. Descriptions of the schemes and results of 1D OAT systems with one surface access are discussed in [25–29]. OAT in backward mode utilizing laser irradiation and a piezoelectric receiving transducer was developed in [25, 28]. It was referred to as "front surface transducers" (FST). Details of the construction, sensitivity, and limitations of one type of FST were described in [22], and its application for tissue diagnostics was described in [25]. More complicated 2D systems are presented in [30–39]. These 2D imaging systems include an array receiving unit or other means of simulating the array. The abilities of LOIS and FST to diagnostic cancer at different stages are described in [25, 28, 32, 33, 36–39]. In this paper, the

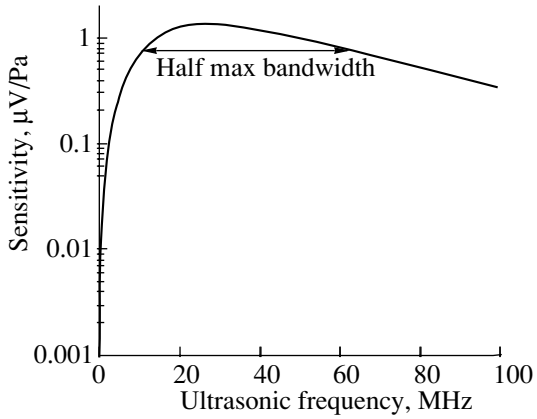

Fig. 3. Spectral sensitivity of CONOAT.

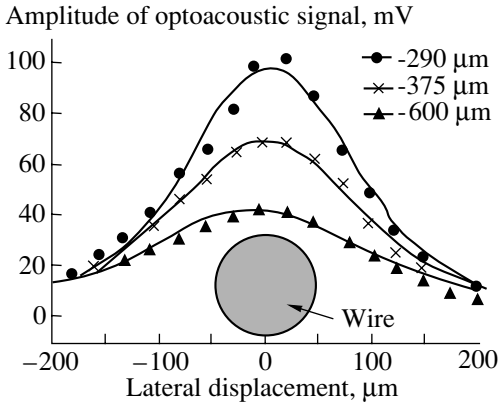

Fig. 4. Lateral resolution of CONOAT.

usage of these two OA systems with real biological tissues is discussed.

2. 1D OPTOACOUSTIC TOMOGRAPHY

2.1. Front Surface Transducer for 1D Imaging

In a continuous effort to develop an imaging modality with high spatial resolution and a sufficient depth of monitoring [21, 40–43], optoacoustic front surface transducers (FST) operating in backward mode were designed. FST enables one to detect acoustic profiles at the site of laser irradiation. Optoacoustic detection in backward mode allows imaging of tissues accessible from only one surface (such as skin surfaces). Optoacoustic tomography is based on short-pulse optical generation of acoustic signals with profiles resembling profiles of absorbed energy distributions in tissue, on detection of these acoustic signals with wide-band acoustic transducers, and on reconstruction of tissue structural images. This technology was tested in biological tissue in vitro and in vivo [25, 28].

The general scheme of front surface transducers (FST) is shown in Fig. 1. The detected OA signal contains information on tissue structure in the volume-absorbed laser energy. Actually, OA signal detected with FST presents an A-scan in the direction perpendicular to the transducer surface. This is its 1D information. To obtain a 2D image, the front surface transducer is scanned along the surface of the tissue.

2.2. Confocal Optoacoustic Transducer

The confocal optoacoustic transducer (CONOAT) was developed as a continuing effort to achieve better lateral resolution of FST. Therevious model of FST could achieve a lateral resolution of up to 250 μm. CONOAT is a novel imaging modality with optical and acoustic lens utilized for detecting in-depth optoacoustic profiles from a narrow cone of laser-irradiated tissue. The schematic diagram of CONOAT is presented in Fig. 2. Pulsed laser radiation was delivered to the CONOAT via optical *fiber* and focused by a condenser (*GRIN*-gradient index) lens onto the *tissue surface* of a medium under investigation through an *optoacoustic lens*. Ultrasonic waves induced in the tissue by laser pulses and propagated backward through the *optoacoustic lens* were transformed with the optoacoustic lens into a plane wave propagating onto the ring-shaped PVDF *piezoelectric detector*. The combination of flat piezotransducer and optoacoustic lens was aimed at obtaining a focused receiving ultrasonic transducer with a narrow and long waist of the focal zone right under the irradiated tissue surface. A charge preamplifier was used to transform acoustic transducer signals into amplified electronic signals for further data acquisition and processing.

2.3. In-Depth Resolution of CONOAT

The main difficulty involved in optoacoustic tomography is associated with correct detection of acoustic signals with high temporal resolution. 1D OAT utilizing FST (including CONOAT) could be referred to as optoacoustic microscopy because it could achieve an in-depth resolution up to several micrometers. In-depth resolution is a resolution in the direction perpendicular to the surface of the transducer. *In-depth resolution* is connected with the temporal resolution of acoustic signal detection Δt by the following expression: *in-depth resolution* = $c_0\Delta t$, where c_0- is the speed of sound in the medium under investigation. The temporal resolution of the detecting transducer is determined by the frequency band of the transducer. The in-depth resolution of the system is also limited by the laser pulse duration. The absolute sensitivity of CONOAT is presented in Fig. 3. The bandwidth of the CONOAT allows registration of acoustic signals with a temporal resolution better than 5 ns. Therefore, the temporal resolution of acoustic signal detection is defined by the laser pulse duration. In the case where laser pulse duration τ_L = 10 ns,

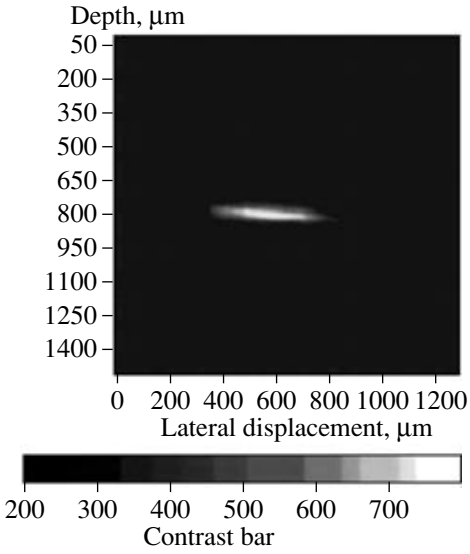

Fig. 5. Optoacoustic image of human hair. 2D image of a hair in a polysterene spheres aqueous solution made with CONOAT. Laser irradiation at second harmonic of Nd-YAG laser ($\lambda = 532$ nm) was focused to a 400-μm diameter spot on the transducer surface. The scattering coefficient of the solution was 10 cm^{-1}. The hair diameter was ~80 μm.

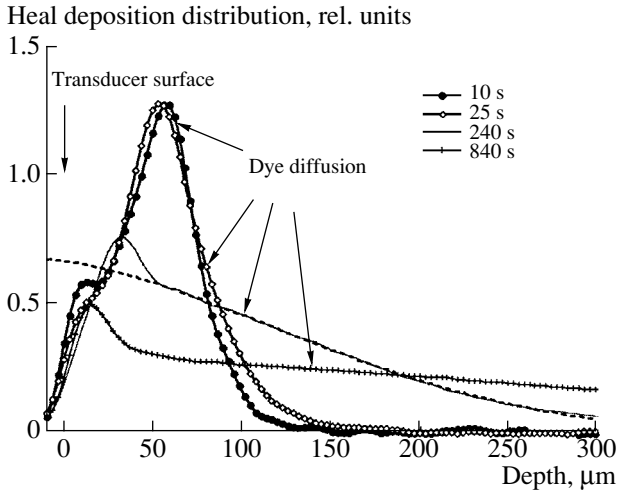

Fig. 6. Invasion of red dye water solution in egg white. Optical attenuation distribution at $\lambda = 532$ nm for different invasion times (10, 25, 240, and 840 s after dye solution application) vs. depth. The dashed line is the fit to the plot corresponding to an invasion time of 240 s. The fit is proportional to $\exp(-z^2/l_d^2)$.

the in-depth axial resolution for biological tissue ($c_0 \sim 1.5 \times 10^5$ cm/s) equals 15 μm.

2.4. Lateral Resolution of CONOAT

Lateral resolution of FST is defined as a combination of the laser spot size at the surface of the medium under investigation (depending on the optical irradiation system) and the resolution of the detecting system (depending on the acoustic transducer size). For CONOAT, the lateral resolution depends on the in-depth resolution and numerical aperture of the optoacoustic lens. For determinations of lateral resolution of CONOAT, aluminum wire 0.1 mm in diameter was placed into the scattering medium at different depths. The scattering medium was polysterene latex beads with an average diameter of 0.76 μm. The scattering coefficient of the beads water solution was 10 cm^{-1}. The OA signal amplitude is given in Fig. 4 as a function of the lateral coordinate. The full width at 1/e of the amplitude equals 210 μm for a depth of 290 μm as measured from the curve in Fig. 4. The dependency widened with the depth of detection. Therefore, lateral resolution decreases with depth as the optoacoustic cone of detection widens.

To demonstrate the spatial resolution of the transducer, optoacoustic imaging of human hair was carried out. Hair with a diameter of 80 μm was placed in water and irradiated with green laser pulses. Scanning across the hair axis was performed with a lateral step of 25.4 μm. Thermal source reconstruction was performed by deconvolution of the OA signal detected with the OA signal from the object with strong (surface) absorption generated in similar conditions (same wavelength, surrounding medium, etc.). The created image is presented in Fig. 5. The circuit cross section of the hair resembles an ellipse with an axis ratio of about five, which corresponds to a numerical aperture of the optoacoustic lens NA ~ 0.25.

2.5. Real-Time Optoacoustic Monitoring of Substance Penetration in Tissue

2.5.1. Drug penetration in homogeneous porous medium

We employed denatured egg white as a model object for investigating passive drug penetration in a homoge-

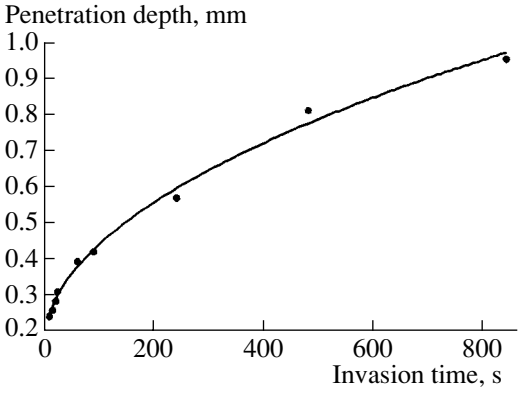

Fig. 7. Dye penetration depth in denatured egg white as a function of invasion time. Dots are experimental data. The solid line is the fit (2) of the data.

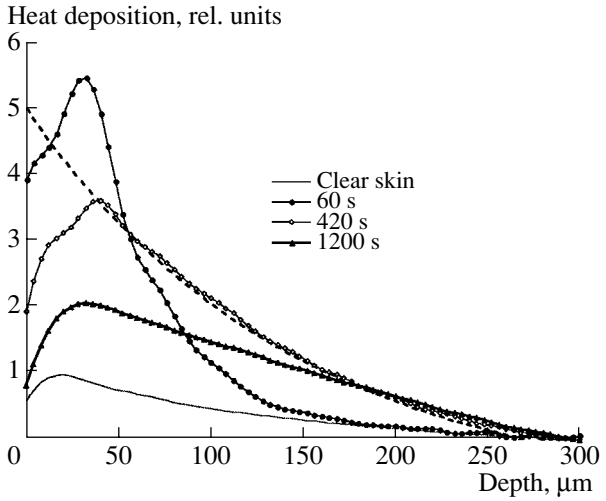

Fig. 8. Invasion of red dye water solution in porcine skin ($\lambda = 532$ nm). Optical attenuation distribution for different invasion time. Dashed line is an exp(–Sz) fitting to the plot corresponding to an invasion time of 420 s.

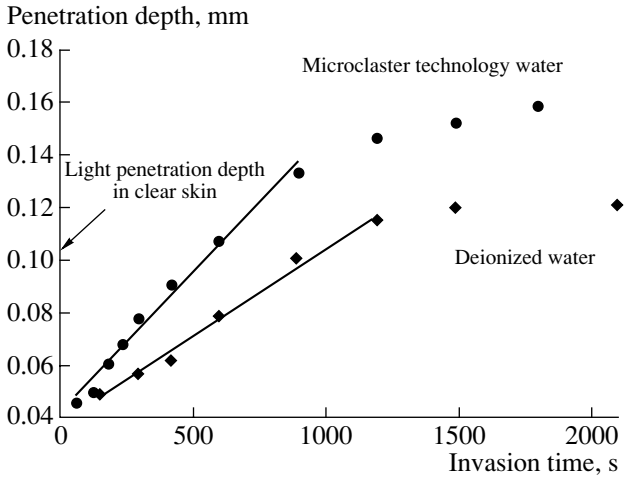

Fig. 9. Propagation of the dye dissloved in water with different surface tension in porcine skin.

neous porous medium. A red dye deionized water solution was applied to the egg-white surface. The OA signal excited by the second harmonic of an Nd:YAG laser was detected with an FST-10. Measurements were made during 15 min after dye application. Signals after deconvolution presenting the distribution of heat deposition are given in Fig.6. The signal from the transducer surface, $z = 0$, arrives at a certain known time corresponding to the ultrasonic transit time through the optoacoustic prism. The invasion of the dye forms the maximum of heat deposition at some depth beneath the surface (50–60 μm for $t < 25$ s). Then, the dye propagates deeper due to diffusion. Nevertheless, some amount of dye remains at the surface (maximum at the depth 10–50 μm for invasion time $t = 240$, 840 s).

The trailing edge of the distributions is determined by diffusion, and their shape corresponded well to the Gaussian curve (the fit is represented as the dashed line in Fig.6):

$$C_d(t, z) \sim \sqrt{\frac{1}{Dt}}\exp\left(-\frac{z^2}{4Dt}\right), \quad (1)$$

where C_d is the concentration of the dye and D is the diffusivity of dye into the egg white. According to (1), the dye penetration depth is

$$l_d = 2\sqrt{Dt}. \quad (2)$$

The penetration depth vs. invasion time is depict in Fig. 7; experimental points correspond well to the curve for $D \approx 3 \times 10^{-6}$ cm^2/s.

2.5.2. Penetration of contrast agent into porcine skin

Penetration of red food dye solution in deionized and microclaster water into porcine skin was investigated with the second harmonic of an Nd:YAG laser ($\lambda = 0.53$ μm). The distributions of heat deposition for various times of invasion for the deionized water solution is presented in Fig. 8. They look similar to that in Fig. 7 obtained for egg white, but the trailing edges of the curves coincide with an exponential law (the fit is represented as the dashed line):

$$C_d(t, z) \sim \exp(-S(t)z). \quad (3)$$

A similar dependence was found for the penetration of a microclaster water solution of red dye into porcine skin.

The penetration depth vs. invasion time for both solutions is presented in Fig.9. For clear porcine skin, the penetration depth was ~100 μm. Just after the application of the solution, the penetration depth falls 2.5 times due to additional light absorption in the dye. With the invasion time, the penetration depth rises up

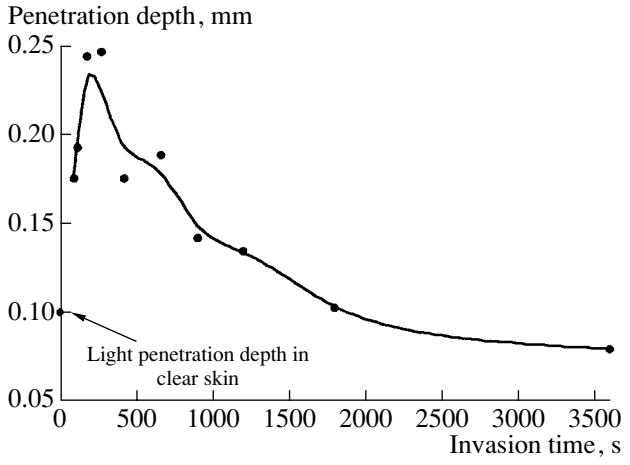

Fig. 10. Invasion of body lotion in porcine skin. Light penetration depth vs. treatment time.

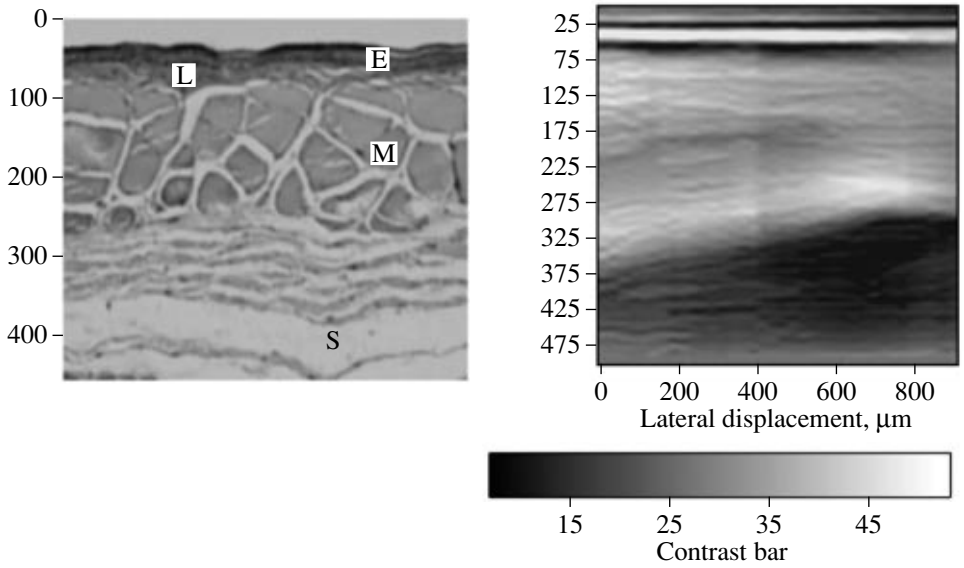

Fig. 11. Histological section and optoacoustic image of hamster normal cheek pouch. Normal buccal mucosa pouch is characterized by a layered structure with distinct layers: keratin on top of epithelium (E), lamina propria (L) muscle fiber mucosa (M), submucosa connective tissue (S).

and then turns to saturate. The velocity of migration $d(S^{-1})/dt$ for the microclaster water solution (11×10^{-5} mm/s) is 1.6 times higher than that for the deionized water solution (6.5×10^{-5} mm/s). The difference in migration velocity can be connected with the difference in the surface tension of the solutions.

Invasion of a lipophilic substance (body lotion) into porcine skin was investigated at the third harmonic of an Nd:YAG laser ($\lambda = 0.355$ μm) to provide sufficient absorption of light in the agent. The trailing edge of the heat deposition distribution also has exponential shape. The dependence of penetration depth vs. time of invasion is given in Fig. 10. After the application of the agent, the light penetration depth rises and reaches a maximum at 5 min, and then the penetration depth slowly drops with a decay time ~13 min. Application of lotion makes the skin more transparent to light due to low mismatch between the refraction coefficients of the skin and contrast agent.

The results presented above were obtained in vitro, but the same investigations could be performed in vivo. The optoacoustic technique in backward mode provides one side access to the tissue; therefore, its inherent advantage is the investigation of tissue in vivo.

2.6. CONOAT for Cancer Diagnostics

Optoacoustic tomography makes it possible to investigate the distribution of light absorption in the depth of a turbid medium. CONOAT gives only an A-scan of this distribution; to obtain a 2D pattern, scanning of CONOAT along the surface of the medium under testing can be employed. This scheme can be successfully used for the investigation of layered tissue. Normal mucous tissue in the digestive system has well-defined layers with different optical absorption. They are the epithelium, lamina propria, muscle fiber mucous, and submucous connective tissue. A process of cancer development leads to gradual destruction in the layered structure. The earliest stages of cancer are characterized by hyperplasia and an irregularly increased thickness of the epithelium. Then, the epithelial layers become more and more thick and have rare and irregular breaks. A more prominent stage of cancer shows a completely irregular pattern and loss of the layered structure.

Two images are presented in this paper. Figure 11 depicts a microscopic histology section (left) and the corresponding optoacoustic image of a normal hamster cheek pouch (right). Both the histology and the optoacoustic tomography display distinct layers that correspond to keratinized, stratified squamous epithelium (E), a very thin basal membrane separating the epithelium from the mucous of lamina propria (L), muscle fiber mucous (M), and submucous connective tissue (S). The progression of carcinoma development was observed in all animals in the presence of invasive carcinoma. Hamster pouch treated with DMBA for 12 weeks showed structural changes characterized as multiple carcinomas in situ and invasive carcinomas. Scanning across the lesion area was performed, and an optoacoustical image was reconstructed. A typical optoacoustic image showing invasive carcinoma and the corresponding histology H&E section are displayed in Fig. 12.

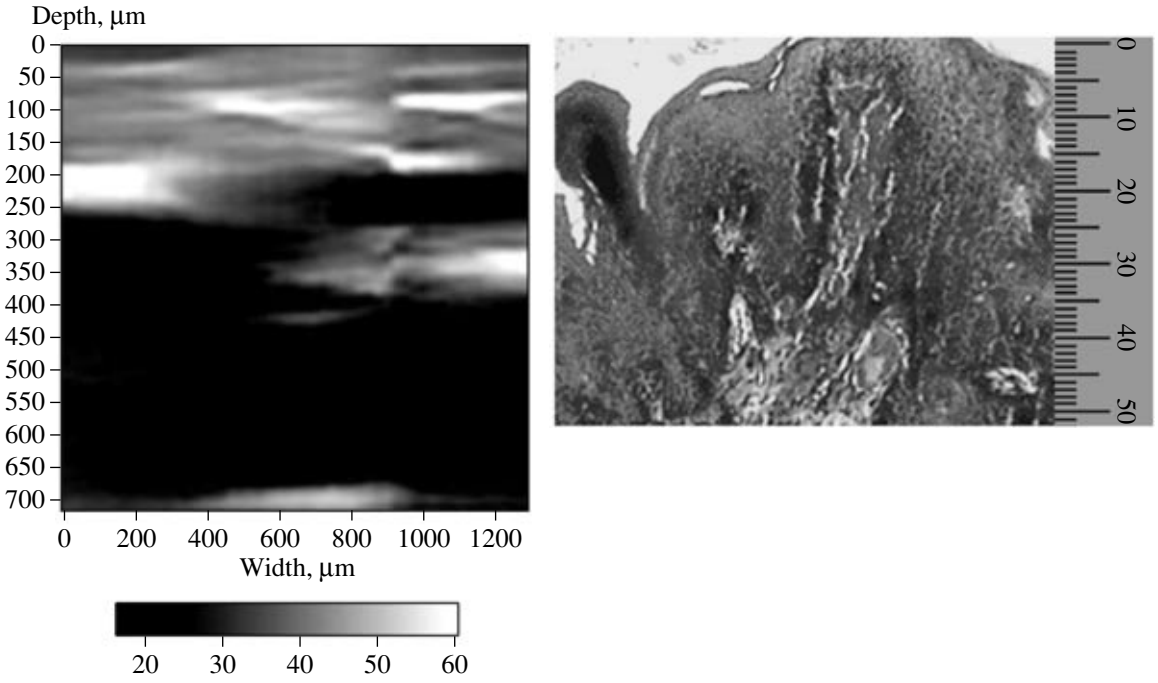

Fig. 12. H&E stain of DMBA model treated during 12 weeks (right) and the corresponding optoacoustic image (left). Histological section of the hamster pouch shows invasive carcinoma. The tumor nests have an irregular outline with infiltrative borders.

3. 2D LASER OPTOACOUSTIC TOMOGRAPHY

3.1. Principles of Operation

The optoacoustic tomography utilizes analysis of the profiles of acoustic signals induced by laser pulses in tissue. Application of the time-resolved ultrasonic detection in optoacoustic tomography instead of detection of photons in optical tomography helps to overcome problems associated with strong light scattering in biological tissues and to improve the depth of monitoring, sensitivity, and spatial resolution [32, 33, 42, 44]. Inhomogenieties with dimensions of 1.5–15 mm irradiated with laser pulses are manifested as sources of acoustic waves with ultrasonic frequencies of ~1 MHz to ~100 kHz. Such ultrasonic waves can propagate in biological tissues with insignificant attenuation [21, 32].

3.2. The Problem of Laser Optoacoustic Tomography

Let us consider the case of thermooptical excitation of acoustic waves in a homogeneous medium with a coefficient of optical absorption μ_a. The temporal integral of acoustic pressure detected by the transducer located at the point $\mathbf{r}$ can be expressed in the following form [45]:

$$u(\mathbf{r}, t) = \int_{-\infty}^{t} p(\mathbf{r}, t')dt' = \frac{\beta}{4\pi C_p}\int_V \frac{\mu_a(\mathbf{r}')I(\mathbf{r}')L\left(t - \frac{|\mathbf{r}-\mathbf{r}'|}{c_s}\right)}{|\mathbf{r}-\mathbf{r}'|}d\mathbf{r}', \quad (4)$$

where β is the thermal coefficient of volume expansion, C_p is the specific thermal capacity of the medium, and L is the laser pulse shape function.

The integral is calculated over the entire space. This means that the acoustic pressure $p(\mathbf{r}, t)$ at the time moment t and in the point $\mathbf{r}$ is determined by the thermal sources located in the spherical layered volume with radius $|\mathbf{r} - \mathbf{r}'|$ and thickness $d\mathbf{r}'$. Acoustic waves arrive at the measurement point $\mathbf{r}$ with time delay $|\mathbf{r} - \mathbf{r}'|/c_s$. If the laser pulses are sufficiently short, then the generation of thermal sources may be considered instantaneous and the laser waveform function can be expressed in the form $L(t) = \tau_L\delta(t)$, where τ_L is the laser pulse duration and $\delta(t)$ is the delta function. Equation (4) for short laser pulses can be written in the following form:

$$u(\mathbf{r}, t) = \frac{\beta}{4\pi C_p}\int_V \frac{\mu_a(\mathbf{r}')F(\mathbf{r}')\delta\left(t - \frac{|\mathbf{r}-\mathbf{r}'|}{c_s}\right)}{|\mathbf{r}-\mathbf{r}'|}d\mathbf{r}', \quad (5)$$

where F is the laser fluence. Let the surface Σ be a spherical surface of radius R with its origin at the position of the receiving transducer. The radius of the sphere is defined by the time of sound propagation from the surface to the transducer. Vector $\mathbf{R}$ can be presented as $\mathbf{R} = c_s t\mathbf{n}$, where $\mathbf{n}$ is the unit vector of the surface element $d\Sigma$. Thus, the temporal integral of acoustic pres-

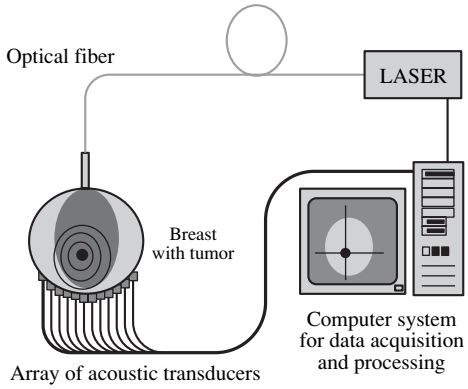

Fig. 13. Schematic diagram of clinical LOIS.

sure can be expressed as

$$u(\mathbf{r}, t) = \frac{\beta}{4\pi C_p c_s t}\int_{\Sigma} Q(\mathbf{r} + c_s t\mathbf{n})d\Sigma, \qquad (6)$$

where function $Q(r) = \mu_a(r)F(r)$ describes the spatial distribution of the thermoacoustic sources.

Equation (6) can be considered the fundamental equation for optoacoustic tomography. The temporal integral of the pressure profile detected by the transducer at time t is a superposition of thermal sources located on a sphere of radius $R = c_s t$. The product of the light absorption coefficient and light fluence at this spherical surface determines the acoustic amplitude of the thermal source.

An image reconstruction algorithm based on a Radon transform with a limited set of data was proposed for optoacoustic tomography [46]. However, this method does not yield satisfactory resolution even with a significant number of transducers employed. We adopted a radial back-projection algorithm that was earlier developed for ultrasound imaging [47]. For the reconstruction of 2D optoacoustic images, we used integrated signals and projected them back onto the 2D grid taking into account the directivity pattern (angle of acceptance) of each transducer. The entire image field resulting from the radial back-projection algorithm can be written in the following form:

$$\xi(\mathbf{r}) = \sum_{n=1}^{m} u_n(|\mathbf{r} - \mathbf{r}_n|/c_s)|\mathbf{r} - \mathbf{r}_n|, \qquad (7)$$

where u_n is the integrated signal of the nth transducer, $\mathbf{r}_n$ is the radius vector of the nth transducer, and m is the number of transducers in the array. The image represents the distribution of the product of the thermoacoustic efficiency, optical absorption, and absorbed laser energy.

3.3. Laser Optoacoustic Imaging System

A schematic diagram of the LOIS is shown in Fig. 13. An Nd:YAG laser (Big Sky Lasers, MA) operating at a wavelength of 1064 nm was used as a source of near-infrared pulses of 10-ns duration. The repetition rate of laser pulses was 20 Hz. A quartz optical fiber was employed for the laser pulse delivery to the tissue surface. A telescope was used to expand the laser beam from the fiber and to deliver a parallel beam 1 cm in diameter to the skin surface.

The array of 32 rectangular piezoelectric transducers with dimensions of 1.5×12 mm and a distance of 4 mm between the transducers was employed in the LOISs. The frequency band of each transducer was 0.05–6 MHz. The transducers were located on an arc surface 120 mm in diameter. A limited viewing angle of 120° resulted in a reduced lateral resolution of 1.5 mm when compared with the in-depth resolution, 0.8 mm. On the other hand, this geometry provided sufficient resolution in a wide area around the focal zone.

The absolute sensitivity of each transducer in the array was measured. Results of this calibration were used in normalizing signals to the sensitivity of each transducer. The mean sensitivity value for the transducer array was $S = 10$ μV/Pa. Electric capacity of each transducer was approximately $C_{pe} = 40$ pF, which resulted in an effective noise level of 20 μV. So, the detection threshold limited by electric shot noise can be estimated as 2 Pa, which corresponds to 10-μK temperature rise in the test volume.

3.4. LOIS Image Resolution

The resolution of the optoacoustic system is defined by the bandwidth of the ultrasonic detection system. For correct detection of the pulsed optoacoustic waveform excited in an absorbing sphere of radius a, it is necessary to detect optoacoustic signals within a wide ultrasound frequency band up to f_b:

$$f_b = 0.75c_s/a, \qquad (8)$$

where c_s is the speed of sound and f_b is the upper limit of the ultrasonic frequency band in the frequency spectrum of the N-shaped signal emitted by the pixel-size sphere.

Therefore, the following inequality must be satisfied: $f_b < f_{\max}$, where $f_{\max}$ is the upper frequency limit of the ultrasound detector. Using (4) for f_b, one can obtain

$$\Delta z > 1.5\frac{c_s}{f_{\max}}. \qquad (9)$$

In the case of the LOIS, the upper frequency limit was 6 MHz, which provided an axial resolution of 0.38 mm.

The lateral resolution of the LOIS is determined by the axial resolution and numeric aperture of the array transducer. So, the spherical object will be presented by the LOIS as elliptical with a ratio of the axis equal to

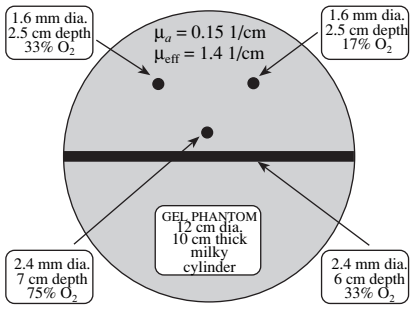

Fig. 14. Collagen gel phantom with artificial blood vessels filled with rabbit blood having various levels of oxygenation. The positions of blood vessels and percent of oxyhemoglobin are shown in the windows. The optical properties of this phantom were similar to the optical properties of the breast at the wavelength of 1064 nm.

~sin(*NA*). This ratio depends on the position of the object at the imaging plane of the transducer: the closer to the transducer, the smaller it will be, and the farther, the greater. For the LOIS, the numeric aperture at the focus is ~0.87.

Therefore, the resolution depends on the position of the tumor relative to the array. In the vicinity of the focal zone (i.e., for the points of location inside the circle of 1-cm radius with its center at the geometrical focus of the array), the resolution is better than 1 mm. In the peripheral part of space, the resolution is about 1–2 mm.

3.5. Time Parameters of LOIS

Data acquisition time in the LOIS equals 1 s for one fiber position. The laser pulse repetition rate is assumed to be 20 Hz, and 16 pulses are employed for averaged acquisitions. Approximately one-third of a second is needed for data processing and back-projected image formation. Image filtration and its optimal processing takes 0.2 s. The total time is 1.5 s.

4. INITIAL TESTS OF CLINICAL LOIS

4.1. Laser Optoacoustic Imaging System

The laser optoacoustic imaging system was tested in various phantoms. As shown in the diagram in Fig. 14, the artificial blood vessels were located at different depths and were placed either parallel or perpendicular to the imaging plane. The transducer array was positioned at the bottom of the image (not shown). A single fiber was used for irradiation at only one location on the surface of the phantom. The phantom was imaged twice: one time with optical fiber positioned at one point on its surface, and the second time at the opposite position (the phantom was rotated 180°).

Two-dimensional images of blood vessels of different diameters filled with blood having different levels of oxygenation is shown in Fig. 15. Whole milk was diluted by water to obtain an effective optical attenuation coefficient of 1.4 cm^{-1} in order to mimic the upper limit of optical scattering in the breast tissue at a wave-

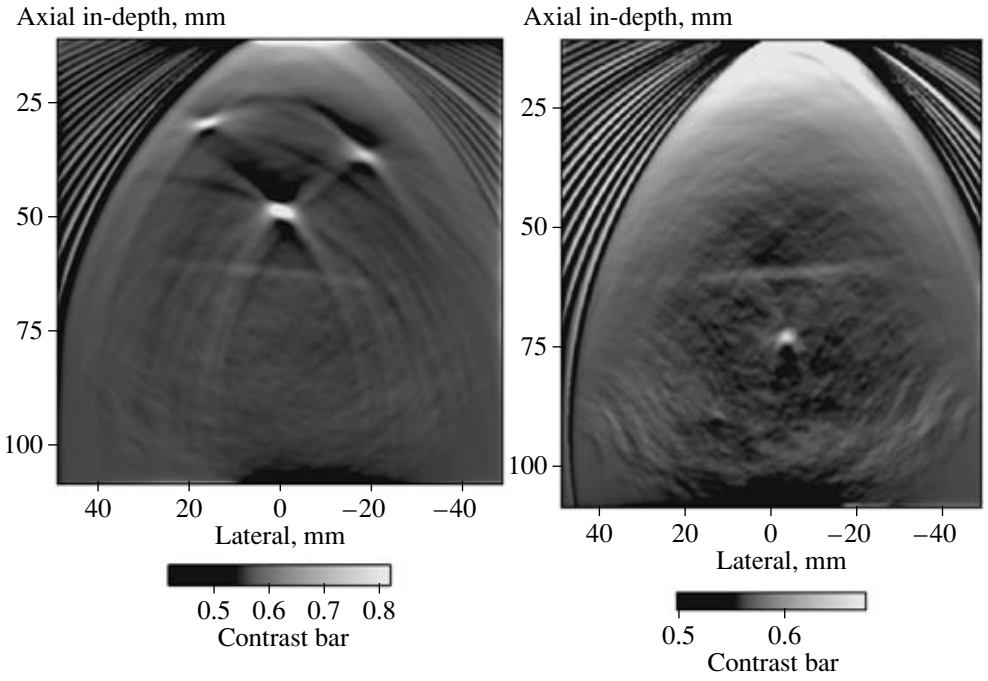

Fig. 15. Optoacoustic image of blood vessels in milky gelatin phantom. The contrast of blood vessels relative to the background is shown in the contrast bar. Depth from the surface is depicted on the left vertical axis of each image.

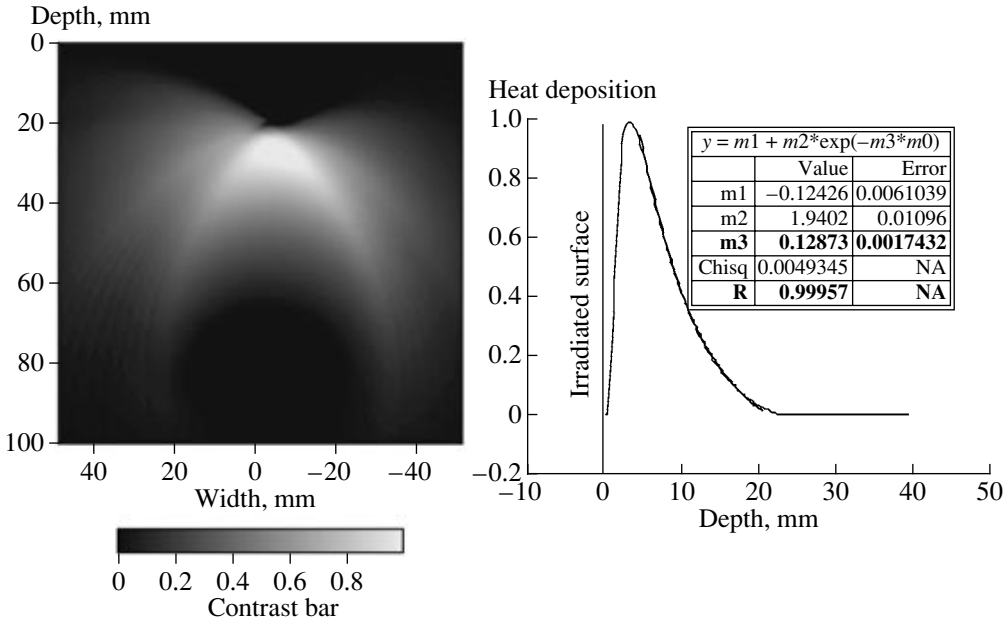

Fig. 16. Optoacoustic image of human arm in the area of byceps (left panel) and in-depth cross section of this image resembling the profile of absorbed optical energy (right panel). The effective optical attenuation coefficient, $\mu_{eff} = 1.28$ cm^{-1}.

length of 1064 nm. Optical absorption coefficients of blood in blood vessels varied from 0.8 to 4.0 per cm depending on the oxygen content. The surface position is visible as a bright area on the images. The first image was reconstructed using optoacoustic signal integrals filtered through a low frequency filter in order to remove the exponential trend associated with effective optical attenuation (Fig. 15, left). The second image was not filtered through a low frequency filter in order that the exponential profile of light distribution in the phantom could be observed (Fig. 15, right).

The image of the blood vessel cross sections differs from the correct circular shape. This is described by a limited numeric aperture of the transducer (see Section 3.3). An increase in the acceptance angle for the blood vessel located farther from the irradiation site and closer to the detector array resulted in a better reproduction of its circular cross section in the image, as is clearly depicted in Fig. 15 (right panel), which shows an image of a blood vessel in the near zone. The angle of acceptance in this case is about 180°, and, as a consequence, the shape of the image highly correlates with the real shape of the circle. Note that our image reconstruction algorithm allows accurate reproduction of spherical objects and cylindrical objects (see the blood vessel in the center in the horizontal direction). Thus, we may predict that objects with random shapes will be correctly reproduced on LOIS images.

All blood vessels were clearly resolved and depicted as separate objects. The relative position of the blood vessels as depicted on the optoacoustic images accurately resembles their position, and their depths are in good agreement with their real location. This imaging experiment demonstrated a sufficient sensitivity of the LOIS for detection of blood vessels at a depth of over 75 mm in an optical, strongly scattering and absorbing phantom. The brightness of the blood vessel images was proportional to the amount of absorbed optical energy, which, in turn was proportional to the level of blood oxygenation in each vessel.

4.2. Quantitative Optoacoustic Imaging

Optoacoustic tomography visualizes the spatial distribution of absorbed optical energy in tissue. However, distortion of optoacoustic signals upon propagation through thick layers of tissue and signal processing may in principle modify the original profile. We tested the possibility of obtaining axial, in-depth profiles of absorbed optical energy from optoacoustic images from human muscle tissue. A human arm was imaged in the byceps area (see Fig. 16) with an LOIS designed for breast cancer imaging.

These experiments demonstrated that quantitative information can be obtained form optoacoustic images. Neither signal correction for acoustic diffraction, reconstruction of the absorbed optical energy distribution from optoacoustic signals, nor correction for sensitivity of individual piezoelectric transducers changed the information quantitatively. The effective optical attenuation coefficient, $\mu_{eff} = 1.28$ cm^{-1}, determined from the exponential fit of the image cross section, was in good agreement with the results of direct measurements of the optical properties in this tissue.

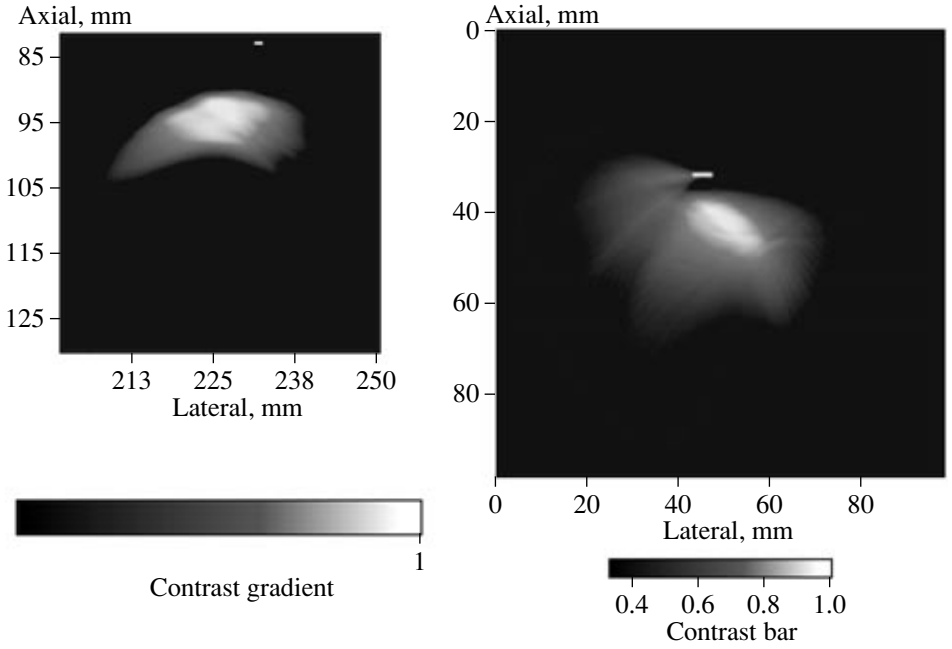

Fig. 17. Optoacoustic image of a malignant tumor obtained in vivo (left, UTMB patient 315221Q), Optoacoustic image of a malignant tumor obtained in vivo (right, UTMB patient 026372P).

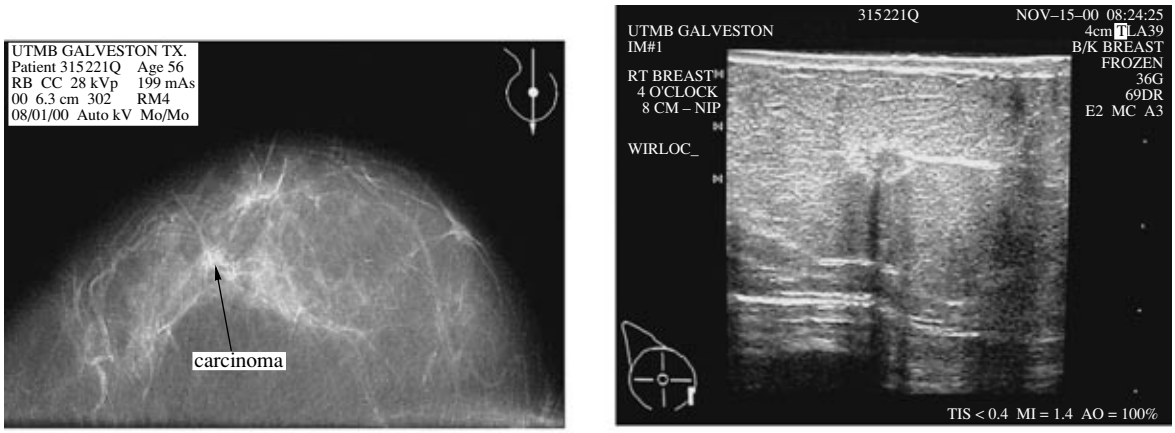

Fig. 18. X-ray mammography image of a cancerous breast (left). There were two suspicious areas on the mammogram; only one of them was a ductal carcinoma. Ultrasound image of the same breast showing a malignant tumor. UTMB Patient 315221.

4.3. Imaging Breast Cancer In Vivo

Eligible patients were chosen from a group of patients scheduled for radical surgical mastectomy with breast cancer diagnosed with x-ray mammography or a combination of x-ray mammography and other imaging modalities (ultrasound, MRI) and biopsy. The patients were imaged in the surgery room before surgery. Two-dimensional optoacoustic images were acquired in several locations on the breast with cancer. Irradiation with 512 pulses from a nanosecond Nd:YAG laser operating at a wavelength of 1064 nm was performed only at one site on the skin surface of the breast. The optoacoustic transducer array was placed on the opposite side of the breast approximately beneath the point of irradiation. The irradiation point was placed approximately above the area suspected of being a tumor. The exact location of tumors was not known prior to the optoacoustic imaging procedure; however, the approximate location could be determined from the mammogram. Tumors were sometimes palpable, and biopsy incision was visible on the spared segment of skin. However, some tumors were not palpable and located deep within the breast. Two exemplary optoacoustic images of breast carcinoma are presented in Fig. 17.

The main conclusion that could be made from clinical experiments on breast cancer patients is that optoacoustic tomography provides enhanced contrast between normal tissues and cancerous tumors. This contrast varies however: no one tumor of five tumors examined had a contrast of less than one; i.e., the optoacoustic amplitude is twice as high in tumors relative to a normal background. The optoacoustic images presented in Fig. 17 depict details of tumor structure based mainly on the optical properties of cancerous tissues. The location of the tumors inside the breast and the tumor dimensions were also accurately determined from the optoacoustic images and confirmed through comparison with x-ray mammography and ultrasound and pathological examination (see Fig. 18). Figure 18 presents x-ray mammography and ultrasound images of a breast with a malignant tumor, which is depicted in the optoacoustic image in Fig. 17 (left). The position of the tumor relative to the skin surface was better determined from the ultrasound image. However, the detailed structure of the tumor was better visualized in the x-ray mammography image. On the other hand, the x-ray image depicted two areas suspicious of being cancerous and only one area contained a malignant tumor (as determined by a pathology study). The tumor core brightly displayed in the optoacoustic image was not visible in neither x-ray or ultrasound images but was confirmed after subsequent pathology examination. The dimension of the tumor core can be estimated as 10×7 mm. The tumor was detected at a depth of 11 mm from the surface (the irradiated point on the surface is marked by the dash in Fig. 17). The contrast between the tumor and surrounding normal tissues in this image exceeds 1.2. The contrast in the ultrasound image and x-ray mammography image of the same tumor did not exceed 0.1. The resolution of the image visualization with the LOIS (~1 mm) was comparable with that of x-ray mammography and ultrasound. The results of comparison between optoacoustic, ultrasonic, and x-ray radiography images for patient 026372 (see Fig. 17, right) and for the other three patients were qualitatively similar.

5. CONCLUSIONS

Time-resolved laser optoacoustic tomography was proposed and shown feasible for noninvasive monitoring of drug and contrast agent delivery into the skin. The spatial resolution achieved upon visualization of the absorbed optical energy distribution is determined by the frequency band and numeric aperture of the ultrasonic detection system and can be as high as 15–50 μm. High sensitivity of the optoacoustic detection permitted monitoring of low concentrations of optically absorbing or scattering–reducing solutions in a turbid medium. The lowest value of the product of the absorption coefficient and laser fluence detectable with the current design of the optoacoustic front surface transducer was $\mu_a F = 7$ cm^{-1} μJ. The presented results demonstrated that the proposed optoacoustic monitoring is a promising technique for monitoring layered biotissue.

The first clinical prototype of the laser optoacoustic system for 2D imaging of the breast in vivo was developed and employed for detection of breast cancer in patients. The system was initially tested in various phantoms and demonstrated specifications that make it suitable for high-contrast imaging of human tissue. The sensitivity of the LOIS permits detection of 2-mm blood vessels at a depth of 7.5 cm. The in-depth resolution equaled 0.4 mm, and the lateral resolution was about 1 mm depending on the position of the tumor relative to the transducer array. Quantitative information on the distribution of absorbed optical energy can be obtained from optoacoustic images.

ACKNOWLEDGMENTS

This work was supported by the National Cancer Institute (grant no. R29-CA80221), DOD Breast Cancer Research Program, US Army (grant no. DAMD17*99-1-9404) and US Civilian Research and Development Foundation (grant no. RP2–2109), and the Russian Foundation for Basic Research (project no. 02-02-08008).

REFERENCES

1. Bell, A.G., 1880, *Am. J. Sci.*, **20**, 305.
2. Veyngerov, M.L., 1938, *Dokl. Akad. Nauk SSSR*, **9**, 9.
3. Gorelik, G.S., 1946, *Dokl. Akad. Nauk SSSR*, **54**, 779.
4. White, R.M., 1963, *J. Appl. Phys.*, **34**, 2123.
5. Askar'yan, G.A., Prokhorov, A.M., Chanturiya, G.F., and Shipulo, G.P., 1963, *Zh. Eksp. Teor. Fiz.*, **44**, 2180.
6. Carome, E.F., Clark, N.A., and Moeller, C.E., 1964, *Appl. Phys. Lett.*, **4**, 95.
7. Cleary, S.F. and Hamrick, P.E., 1968, *Va. J. Sci.*, **19**, 228.
8. Burmistrova, L.V., Karabutov, A.A., Portnyagin, A.I., *et al.*, 1978, *Sov. Phys. Acoust.*, **24**, no. 5, 369.
9. Karabutov, A.A., Rudenko, O.V., and Cherepetskaya, E.B., 1979, *Sov. Phys. Acoust.*, **25**, no. 3, 218.
10. Karabutov, A.A., Portnyagin, A.I., Rudenko, O.V., and Cherepetskaya, E.B., 1979, *Pis'ma Zh. Tekh. Fiz.*, **5**, 328.
11. Karabutov, A.A., Omel'chuk, N.N., Rudenko, O.V., and Chupryna, V.A., 1985, *Moscow Univ. Bull., Ser. 3*, **26**, 48.
12. Cross, F.W., Al-Dhahir, R.K., Dyer, P.E., and MacRobert, A.J., 1987, *Appl. Phys. Lett.*, **50**, 1019.
13. Cross, F.W., Al-Dhahir, R.K., Dyer, P.E., and MacRobert, A.J., 1988, *Appl. Phys.*, **64**, 2194.
14. Oraevsky, A.A., Jacques, S.L., Esenaliev, R.O., and Tittel, F.K., 1993, *Proc. SPIE*, **1882**, 86.
15. Oraevsky, A.A., 1993, *IEEE LEOS Newsl.*, **2**, 6.
16. Oraevsky, A.A., Jacques, S.L., Esenaliev, R.O., and Tittel, F.K., 1994, *OSA Proceedings on Advances in Optical Imaging and Photon Migration*, March 21–23, 1994, Orlando, Florida, Alfano, R.R., Ed. (Washington, DC: The Society), vol. 21, p. 161.

17. Wolbarsht, M.L., 1981, *Sov. J. Quantum Electron.*, **11** (12), 1623.
18. Gusev, V.E. and Karabutov, A.A., 1993, *Laser Optoacoustic* (New York: Am. Inst. Phys.).
19. Karabutov, A.A., Podymova, N.B., and Letokhov, V.S., 1994, *Opt. Eng. Bull.*, **4**, 22.
20. Karabutov, A.A., Podymova, N.B., and Letokhov, V.S., 1995, *J. Mod. Opt.*, **42**, 7.
21. Karabutov, A.A., Podymova, N.B., and Letokhov, V.S., 1996, *Appl. Phys. B*, **63**, 545.
22. Karabutov, A.A., Savateeva, E.V., Podymova, N.B., and Oraevsky, A.A., 2000, *J. Appl. Phys.*, **87**, no. 4, 2003.
23. Biomedical Optoacoustics, Oraevsky, A., Ed., 2001, *Proc. SPIE*, **3916**.
24. Biomedical Optoacoustics II, Oraevsky, A., Ed., 2000, *Proc. SPIE*, **4256**.
25. Karabutov, A.A., Savateeva, E.V., and Oraevsky, A.A., 1999, *Proc. SPIE*, **3601**, 284.
26. Paltauf, G., Schmidt-Klober, H., Koesti, P.P., *et al.*, 2000, *Proc. SPIE*, **3916**, 240.
27. Kolkman, R.G.M., Piatou, M.C., Hondebrink, E., and de Mul, F.F.M., 2000, *Proc. SPIE*, **3916**, 76.
28. Savateeva, E.V., Karabutov, A.A., Bell, B., *et al.*, 2000, *Proc. SPIE*, **3916**, 55.
29. Viator, J.A., Paltauf, G., Jaques, S.L., *et al.*, 2001, *Proc. SPIE*, **4256**, 16.
30. Kruger, R.A., Liu, P., Fang, Y.R., and Appledorn, C.R., 1995, *Med. Phys.*, **22**, 1605.
31. Hoelen, C.G.A., Pongers, R., Dekker, A., and de Mul, F.F.M., 1998, *Advances in Optical Imaging and Photon Migration*, Fujimoto, J.G. and Patterson, M.S., Eds. (Washington, DC: OSA), vol. 21, p. 386.
32. Oraevsky, A.A., Andreev, V.G., Karabutov, A.A., *et al.*, 1999, *Proc. SPIE*, **3597**, 352.
33. Oraevsky, A.A., Andreev, V.G., Karabutov, A.A., and Esenaliev, R.O., 1999, *Proc. SPIE*, **3601**, 256.
34. Hoelen, C.G.A. and de Mul, F.F.M., 2000, *Appl. Opt.*, **39**, no. 31, 5872.
35. Kruger, R.A., Kisler, W.L., Miller, K.D., and Reynolds, H.E., 2000, *Proc. SPIE*, **3916**, 150.
36. Andreev, V.G., Karabutov, A.A., Solomatin, S.V., *et al.*, 2000, *Proc. SPIE*, **3916**, 36.
37. Beard, P.C. and Mills, T.N., 2001, *Proc. SPIE*, **4256**, 34.
38. Kruger, R.A. and Kisler, W.L., 2001, *Proc. SPIE*, **4256**, 1.
39. Oraevsky, A.A., Karabutov, A.A., Solomatin, S.V., *et al.*, 2001, *Proc. SPIE*, **4256**, 6.
40. Oraevsky, A.A., 1994, *LEOS Newsl.*, **8**, no. 1, 6.
41. Oraevsky, A.A., Jacques, S.L., Esenaliev, R.O., and Tittel, F.K., 1994, *OSA Proceedings on Advances in Optical Imaging and Photon Migration*, March 21–23, 1994, Orlando, Florida, Alfano, R.R., Ed. (Washington, DC: The Society), vol. 21, p. 161.
42. Oraevsky, A.A., Esenaliev, R.O., Jacques, S.L., *et al.*, 1995, *Proc. SPIE*, **2389**, 198.
43. Oraevsky, A.A., Esenaliev, R.O., Jacques, S.L., and Tittel, F.K., 1996, *Proc. SPIE*, **2676**, 22.
44. Esenaliev, R.O., Karabutov, A.A., and Oraevsky, A.A., 1999, *IEEE J. Sel. Top. Quantum Electron.*, **5**, no. 4, 981.
45. Oraevsky, A.A., 1996, *LEOS Newsl.*, **10**, no. 6, 17.
46. Liu, P., 1999, *Proc. SPIE*, **2681**, 285.
47. Ternovoi, K.C. and Sinkov, M.V., 1996, *Introduction to Modern Tomography* (Kiev: Naukova Dumka) (in Russian).